inorganics

MDPI

Article

Decorating Ti_3C_2 MXene Nanosheets with Fe-N_x-C Nanoparticles for Efficient Oxygen Reduction Reaction

Han Zheng, Fagang Wang * and Weimeng Si *

School of Materials Science and Engineering, Shandong University of Technology, Xincunxi Road 266th, Zibo 255000, China

* Correspondence: a_gang@sdut.edu.cn (F.W.); siweimeng@foxmail.com (W.S.); Tel./Fax: +86-533-2781317 (F.W.)

Abstract: Finding alternatives to platinum that exhibit high activity, stability, and abundant reserves as oxygen reduction electrocatalysts is crucial for the advancement of fuel cells. In this study, we first mixed $FeCl_2 \cdot 4H_2O$, 1,10-phenanthroline, and Vulcan XC-72, followed by pyrolysis in a nitrogen atmosphere, to obtain FeNC. Subsequently, we combined FeNC with MXene produce FeNC/MXene composites. The FeNC/MXene catalyst achieved a half-wave potential of 0.857 V in an alkaline medium, exhibiting better oxygen reduction reaction (ORR) activity and durability than commercial Pt/C catalysts. The layered structure of MXene endows the material with a high specific surface area and facilitates efficient electron transfer pathways, thereby promoting rapid charge transfer and material diffusion. The cleavage of Ti-C bonds in Ti_3C_2 at elevated temperatures results in the transformation of MXene into TiO_2, where the coexistence of anatase and rutile phases generates a synergistic effect that enhances both the mass transfer rate and the electrical conductivity of the catalytic layer. Additionally, the unique electronic structure of the FeN_x sites simultaneously optimizes electrocatalytic activity and stability. Leveraging these structural advantages, the FeNC/MXene composite catalysts demonstrate exceptional catalytic activity and long-term stability in oxygen reduction reactions.

Keywords: Fe-N-C catalysts; MXene; Non-Pt catalysts; oxygen reduction reaction

check for updates

Academic Editor: Junxian Liu

Received: 24 April 2025
Revised: 19 May 2025
Accepted: 4 June 2025
Published: 6 June 2025

Citation: Zheng, H.; Wang, F.; Si, W. Decorating Ti_3C_2 MXene Nanosheets with Fe-N_x-C Nanoparticles for Efficient Oxygen Reduction Reaction. *Inorganics* **2025**, *13*, 188. https://doi.org/10.3390/inorganics13060188

Copyright: © 2025 by the authors. Licensee MDPI, Basel, Switzerland. This article is an open access article distributed under the terms and conditions of the Creative Commons Attribution (CC BY) license (https://creativecommons.org/licenses/by/4.0/).

1. Introduction

As the global community increasingly prioritizes energy and environmental issues, hydrogen fuel cells have garnered significant attention [1,2]. In these cells, hydrogen is oxidized through the hydrogen oxidation process, while oxygen undergoes reduction, enabling the conversion of stored energy into electrical energy via the oxygen reduction mechanism [3–5]. However, the ORR is characterized by slow kinetics and necessitates a high overpotential for effective operation. Currently, precious metal-based electrocatalysts represent the most advanced ORR catalysts [6]; however, they possess several limitations, including high costs, a low abundance of the constituent metals, single functionality, and poor stability [7]. Therefore, cost-effective and durable non-precious metal ORR catalysts are vital for improving fuel cell performance and promoting sustainable energy development.

Nitrogen–carbon (M-N-C) materials doped with transition metals are regarded as promising substitutes for commercial Pt/C catalysts [8–11]. The incorporation of transition metals benefits the ORR by weakening the bond strength of key intermediates (OOH*, O*, OH*), as these metals can effectively accept external electrons [12–14]. This phenomenon arises from the three-dimensional electronic orbitals of transition metals, which have the ability to accommodate external electrons. Additionally, the introduction of nitrogen through doping can facilitate the formation of additional active sites,

thereby enhancing the electrochemical efficiency of the catalyst and promoting the ORR. Notably, carbon materials exhibit electrical conductivity, and nitrogen doping can further improve this property, increasing the rate of electron transfer within the catalyst [15,16]. The synergy between transition metals and nitrogen-doped carbon enhances both durability and catalytic activity, leading to improved ORR performance. Among these materials, iron–nitrogen–carbon (Fe-N-C) has attracted considerable attention for its promise as a high-performance alternative to noble metal catalysts like Pt/C [17,18]. Fe-N-C materials offer several advantages, including moderate cost, high conductivity, stability, and high catalytic efficiency [19–22]. However, the pyrolysis process unavoidably induces significant aggregation and the formation of thick catalyst layers, thereby impeding mass transport and ionic conductivity, which ultimately results in suboptimal ORR performance [23]. To overcome this problem, researchers have designed various Fe-N-C catalysts supported on diverse substrates, including covalent organic frameworks (COFs) [24], imidazole zeolite frameworks (ZIFs) [25], and MXene [26,27]. In particular, MXene materials have garnered significant interest for heterogeneous catalysis, attributed to their layered architectures and rich functional groups [28].

MXene ($Mn_{(1-x)}X_{(x+1)}T_x$, where M is an early transition metal, X represents C and/or N, and T denotes surface terminations) is a novel two-dimensional transition metal carbide or nitride. It is widely applied in energy storage and conversion due to its excellent electrical conductivity, hydrophilicity [29,30], and unique surface properties [28,31–33]. However, MXene features a readily stackable sheet structure, which is held together by van der Waals forces and hydrogen bonds [34]. Variations in MXene's lattice structure and surface terminations can significantly alter its electronic properties, allowing the fine-tuning of its surface environment and catalyst interactions [35]. Consequently, MXene could play a pivotal role in enhancing the catalytic activity of Fe-N-C.

In the present study, a composite material was designed, consisting of Fe-N_x-C and Ti_3C_2-type MXene. A series of FeNC/MXene electrocatalysts was prepared, and their electrochemical performance as ORR catalysts in an alkaline medium was investigated. Furthermore, we optimized the pyrolysis temperature of Fe-N_x-C and MXene to achieve the most effective ORR activity. The FeNC/MXene catalyst demonstrates a high half-wave potential of 0.857 V and supports an efficient four-electron ORR pathway. It also exhibits excellent stability and strong resistance to methanol crossover. These FeNC/MXene catalysts meet the necessary criteria for both purity and high performance, and are expected to serve as a cost-effective, efficient, and sustainable alternative to commercial Pt/C catalysts.

2. Experimental Section

2.1. Materials

MAX phase (Ti_3AlC_2) was bought from Jilin 11 Technology Co., Ltd. (Changchun, China). Hydrofluoric acid (40%), methanol (99.5%), and propan-2-ol (99.7%) were purchased from Sinopharm Chemical Reagent Co., Ltd. (Shanghai, China). Iron(II) chloride tetrahydrate and 1,10-phenanthroline were purchased from Macklin chemical reagent. (Shanghai, China). Vulcan XC-72 carbon black was purchased from Cabot Corporation (Boston, MA, USA), and Nafion was obtained from DuPont (Wilmington, DE, USA).

2.2. Synthesis of MXene

1 g of Ti_3AlC_2 was gradually introduced into 20 mL of a 40% HF solution and stirred at 45 °C for 24 h [36]. Following the stirring process, the mixture was subjected to repeated centrifugation with deionized water until the pH reached 6. The precipitate obtained from centrifugation was subsequently collected and vacuum-freeze-dried for 12 h to yield multilayered $Ti_3C_2T_x$.

2.3. Synthesis of eNC/MXene

A total of 120 mg of carbon black (Vulcan XC72) was combined with 8 mL of methanol. In a separate preparation, 22 mg of Iron(II) chloride tetrahydrate was added to 1 mL of methanol, and 60 mg of 1,10-phenanthroline was dissolved in 1 mL of methanol. The three resulting solutions were then combined and stirred thoroughly. The mixture was subsequently placed in an open beaker, where it was continuously stirred at a temperature of 60 °C until complete evaporation of the solvent occurred. Following this, the material was heated in an oven at 80 °C for two hours. The carbon black-containing $[Fephen_3]^{2+}$ was then transferred to a tubular heating furnace and subjected to pyrolysis at 800 °C for three hours, utilizing a heating rate of 5 °C min^{-1} in a nitrogen atmosphere. The final product was designated as FeNC.

To prepare the FeNC/MXene composite, add 30 mg of MXene and 30 mg of FeNC to 20 mL of methanol. Stir the mixture at 60 °C until the methanol has completely evaporated. Subsequently, transfer the resulting mixture to a tube furnace and subject it to pyrolysis in a nitrogen atmosphere at 800 °C for a duration of 2 h.

2.4. Electrochemical Characterization

In this experiment, all electrochemical measurements were performed using a CS2350 electrochemical workstation with a standard three-electrode configuration. A saturated Hg/HgO electrode was used as the reference electrode, a graphite rod as the counter electrode, and a 5 mm diameter glassy carbon rotating disk electrode (RDE) as the working electrode. The electrolyte was 0.1 M KOH, which was saturated with oxygen prior to testing to ensure reliable evaluation of the catalyst's ORR performance. To standardize the results, all potentials were converted to the reversible hydrogen electrode (RHE) scale using the following equation:

$$RHE = Hg/HgO + 0.059pH + 0.098$$

Before testing, the catalyst was prepared into an ink by dispersing 5 mg of catalyst in 200 μL of isopropanol, 780 μL of ultrapure water, and 20 μL of 5% Nafion solution. The mixture was sonicated for 1 h to ensure uniform dispersion. The working electrode was polished with 50 nm Al_2O_3 powder to remove surface impurities. Then, 20 μL of the catalyst ink was drop-cast onto the RDE surface and allowed to dry. Electrochemical activation was performed using cyclic voltammetry (CV) in O_2-saturated 0.1 M KOH at a scan rate of 50 mV s^{-1} over a potential range of 0.1–1.1 V (vs. RHE). ORR activity was evaluated via linear sweep voltammetry (LSV) under O_2-saturated conditions at a scan rate of 10 mV s^{-1} and a rotation speed of 1600 rpm, within the potential range of 0–1.1 V (vs. RHE). To analyze the reaction kinetics, LSV curves were also recorded at various rotation rates (625–2025 rpm). The Koutecky–Levich (K-L) equation was used to calculate the number of electrons transferred (*n*), expressed as

$$j^{-1} = {j_K}^{-1} + {j_L}^{-1} = {j_K}^{-1} + (B\omega^{0.5})^{-1}$$

where B is defined by the following equation:

$$B = 0.2nFC_0{D_0}^{2/3}v^{-1/6}$$

Here, j represents the measured limiting current density; j_K and j_L denote the kinetic and limiting diffusion current densities, respectively; ω indicates the angular velocity of the rotating disk electrode (RDE); n is the number of electron transfers; and F is Faraday's constant (F = 96,485 C mol^{-1}). Additionally, C_0 is the volume concentration of O_2 in

0.1 M KOH (C_0 = 1.2 × 10^{-6} mol cm^{-3}), D_0 is the diffusion coefficient of O_2, which is 1.9 × 10^{-5} cm^2 s^{-1}, and the kinematic viscosity of the electrolyte (γ) is 0.01 cm^2 s^{-1} in 0.1 M KOH. The rotation speed (rpm) is expressed using the constant 0.2.

3. Results and Discussion

3.1. Characterization of FeNC/MXene

Figure 1a presents the X-ray diffraction (XRD) image of the MAX phase and MXene. A distinct diffraction peak at 2θ = 38.4°, indexed as (104), is observed in the MAX phase, attributed to aluminum (Al), which must be fully removed to obtain the MXene [37] layer. The disappearance of the 38.4° peak after 24 h HF etching confirms the complete removal of aluminum and the formation of high-purity, layered MXene. Additionally, new diffraction peaks corresponding to the crystal planes (002), (004), and (006) appear at 2θ values of 8.6°, 17.9°, and 27.1°, respectively [36]. The diffraction pattern provides additional evidence for the successful conversion of Ti_3AlC_2 to Ti_3C_2. Notably, the (002) peak shifts to a lower angle in the MXene phase (2θ = 8.6°), likely due to the increased lattice spacing caused by the expansion of the Ti_3C_2 layers along the (002) plane, thus validating the characteristic accordion-like structure of MXene. As seen in Figure 1b, the XRD image of FeNC exhibits characteristic diffraction peaks corresponding to Vulcan XC72 at angles of 25° and 43° [38]. The XRD plots of FeNC/MXene-1 exhibit characteristic peaks at 27.3°, 35.9°, 41.1°, 43.9°, 54.1°, and 56.5°, which correspond to the (110), (101), (111), (210), (211), and (220) crystal facets of rutile TiO_2 [39]. Additionally, a weak peak at 25.1° corresponds to the (110) crystal facet. The absence of peaks corresponding to Ti_3C_2 in the XRD pattern of FeNC/MXene-1 may be attributed to the dominance of TiO_2 peaks, which hinder the detection of Ti_3C_2. In addition, no diffraction peaks corresponding to iron-based species were observed in the XRD patterns of either FeNC or FeNC/MXene-1, indicating that the iron species were atomically dispersed within the carbon matrix [40]. These Fe-N-C catalysts may interact with TiO_2 nanoparticles, resulting in a synergistic effect [41].

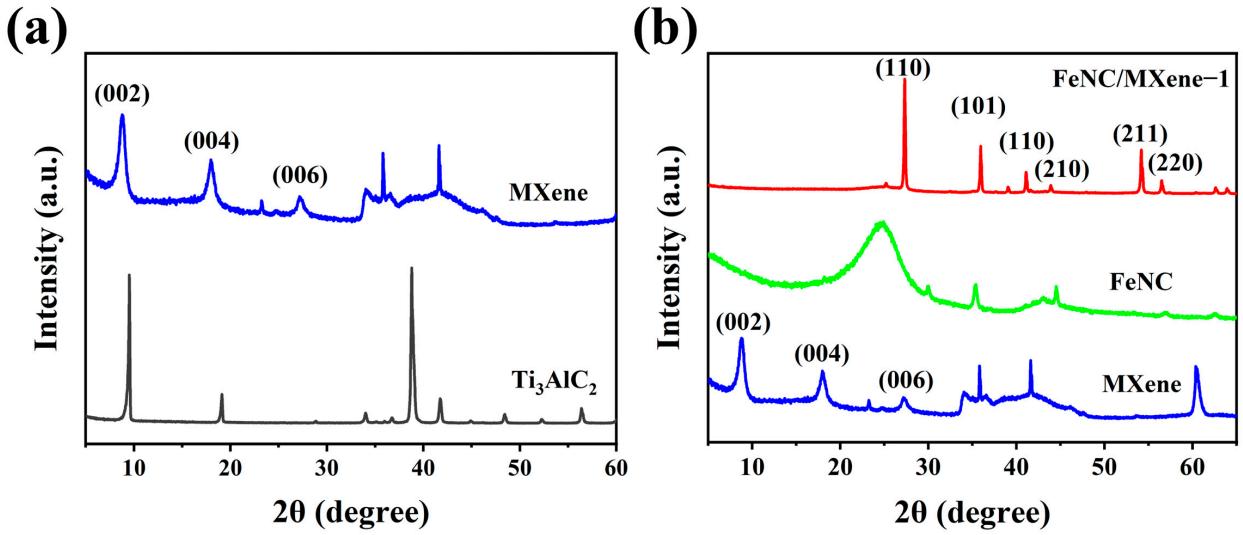


Figure 1. (**a**) XRD pattern of MXene and Ti_3AlC_2; (**b**) XRD pattern of FeNC/MXene-1, FeNC, and MXene.

Figure 2a illustrates the XRD plots of FeNC/MXene at various pyrolysis temperatures. At a pyrolysis temperature of 700 °C, MXene is converted to anatase TiO_2 due to the facile cleavage of the Ti-C bond in Ti_3C_2 at elevated temperatures, leading to the formation of TiO_2. Anatase TiO_2 exhibits a more open crystal structure, a relatively high specific surface area, an abundance of surface defects, and a rich presence of oxygen vacancies,

all of which contribute to its high catalytic activity. When the pyrolysis temperature is elevated to 800 °C, anatase TiO_2 transforms into rutile TiO_2, with the peak intensity of rutile TiO_2 increasing further with higher pyrolysis temperatures, indicating the generation of additional TiO_2. Rutile TiO_2 possesses relatively good electrical conductivity, particularly at high temperatures, which enhances its stability in electrocatalytic reactions characterized by high voltage and current density. The anatase and rutile phases in mixed-phase TiO_2 exhibit a beneficial synergistic effect [42,43]. An optimal ratio of anatase to rutile enhances the mass transfer rate and conductivity of the catalytic layer [44]. As shown in Figure 2b, Raman spectroscopy was conducted to investigate FeNC/MXene at different pyrolysis temperatures. The Raman spectra (Figure 2b) show the D (1340 cm^{-1}) and G (1580 cm^{-1}) bands of carbon crystals, which are associated with defects in the carbon lattice and the vibrations of sp^2-hybridized carbon atoms, respectively. The intensity ratio (I_D/I_G) reflects the surface defects in the carbon film, with values of 1.03 for FeNC/MXene-700, 1.08 for FeNC/MXene-800, and 1.08 for FeNC/MXene-900, indicating that the carbon layer in FeNC/MXene-800 has a higher defect density [45,46].

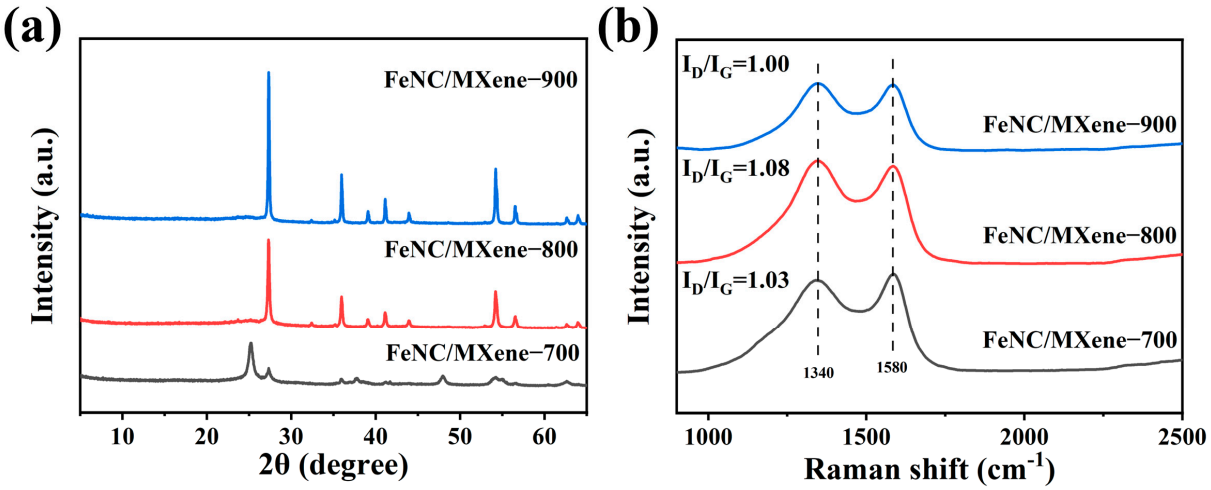


Figure 2. (**a**) XRD pattern and (**b**) Raman spectra of FeNC/MXene-700, FeNC/Mene-800, and FeNC/Mene-900.

The surface morphology of the MAX phase (MXene), FeNC, and FeNC/MXene was observed via scanning electron microscopy (SEM). As illustrated in Figure S1, the MAX phase exhibited closely stacked layers, whereas the MAX phase underwent a successful transformation into an accordion-like (see Figure 3b) MXene layer following 24 h of etching. Figure 3c depicts the FeNC structure without MXene, which exhibits agglomerated particles. Following the doping of MXene into FeNC at a mass ratio of 1:1, the surface of MXene was modified by FeNC particles, as illustrated in Figure 3d. This process retained the lamellar structure of MXene while simultaneously facilitating the dispersion of FeNC clusters, thereby improving the porosity of the material. The dispersion of FeNC clusters over time led to an improvement in porosity. Furthermore, the distribution of FeNC particles in the interlayer of MXene hindered lamellar stacking and enhanced mass transport, greatly improving ORR performance [47].

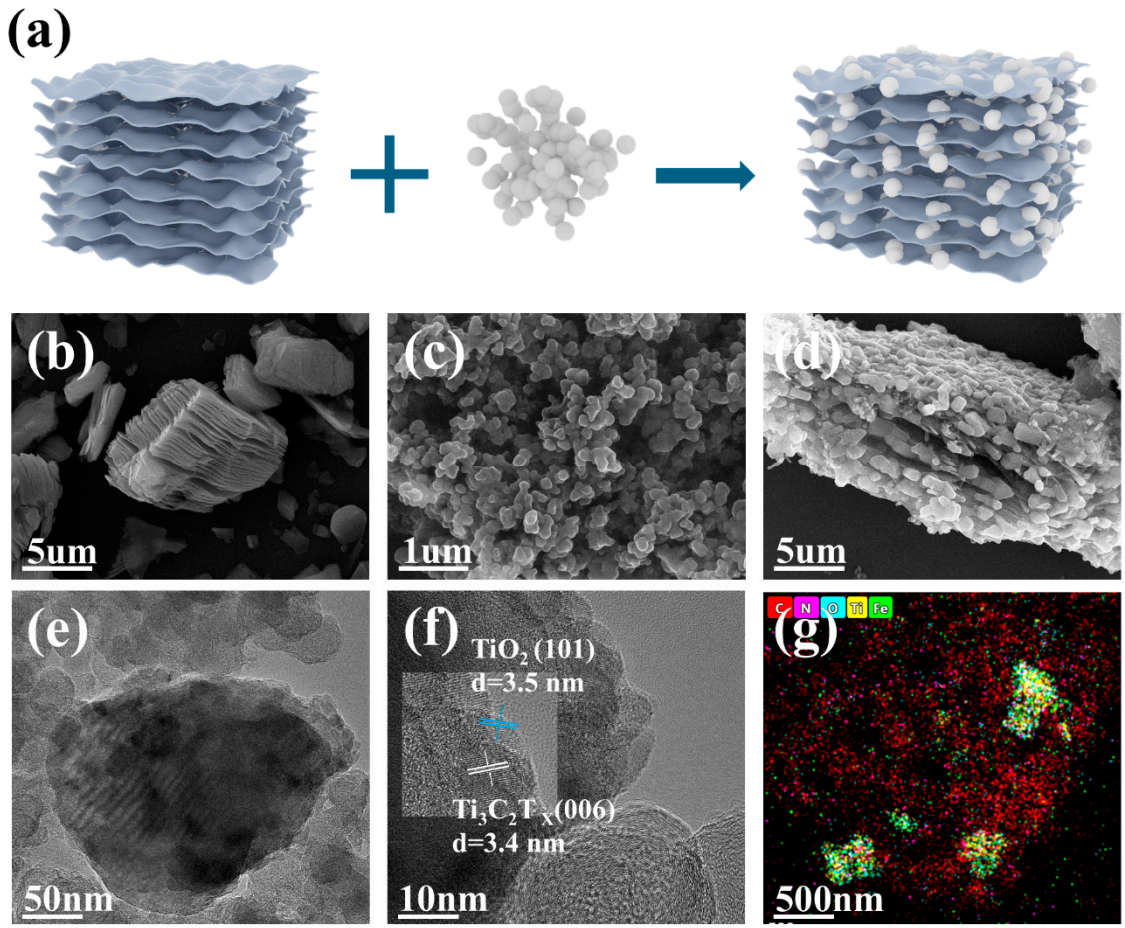


Figure 3. (**a**) Schematic illustration of FeNC/MXene hybridization; (**b**) SEM images of MXene, (**c**) FeNC, and (**d**) FeNC/MXene-1; (**e**,**f**) TEM images of FeNC/MXene-1; (**g**) overlay of the elemental mapping of the energy-scattered X-ray spectra of FeNC/MXene-1.

The figure shows a TEM image of a highly porous FeNC/MXene electrocatalyst (see Figure 3e,f). The TEM image further verifies that the MXene layer covers the FeNC, in agreement with the SEM image. It shows that the edges of FeNC/MXene appear more worn or rough, indicating an increase in porosity. The lattice stripe spacing of TiO_2 has been measured to be 0.35 nm, which corresponds to the (101) crystal plane, and the lattice stripe spacing of $Ti_3C_2T_x$ MXene has been measured to be 0.34 nm, which corresponds to the (006) crystal plane. Additionally, the lack of carbon lattice fringes confirms the amorphous nature of FeNC, which contributes to enhanced resistance to volume change during electrochemical reactions [48]. Furthermore, elemental mapping revealed the presence of C, N, O, Ti, and Fe (see Figure 3g), indicating that MXene and FeNC effectively hybridized to form a novel FeNC/MXene with a unique microstructure, in which the aggregation of metallic Fe atoms can be efficiently avoided during annealing due to the discrete nature of the Fe–phenanthroline complex [49], which is conducive to the formation of high-density and uniformly distributed Fe-N_X sites.

It is hypothesized that the enhanced activity may result from the interaction at the FeNC/MXene interface. The electronic structure of FeN_4 groups, before and after coupling with MXene, was examined using multi-spectral techniques. The X-ray photoelectron spectroscopy (XPS) measurement produced a spectrum confirming the presence of Ti, Fe, N, C, O, and F (see Figure S2). It can be inferred that the signals corresponding to O and F may originate from the hydroxyl and fluorine ends of MXene, respectively. In the pure FeNC spectrum, the $Fe2p_{3/2}$ and $Fe2p_{1/2}$ peaks in the XPS narrow scan are observed at 710.1 eV

and 722.9 eV, respectively. Following coupling with MXene, both peaks shift to 711.8 eV and 725.4 eV, as illustrated in Figure 4a,b. Although the XPS signal of Fe2p is relatively weak, the noticeable shift in the Fe2p peak to higher binding energies suggests a strong interaction between MXene and the FeN_4 component, which significantly diminishes the local electronic density at the Fe center [35].

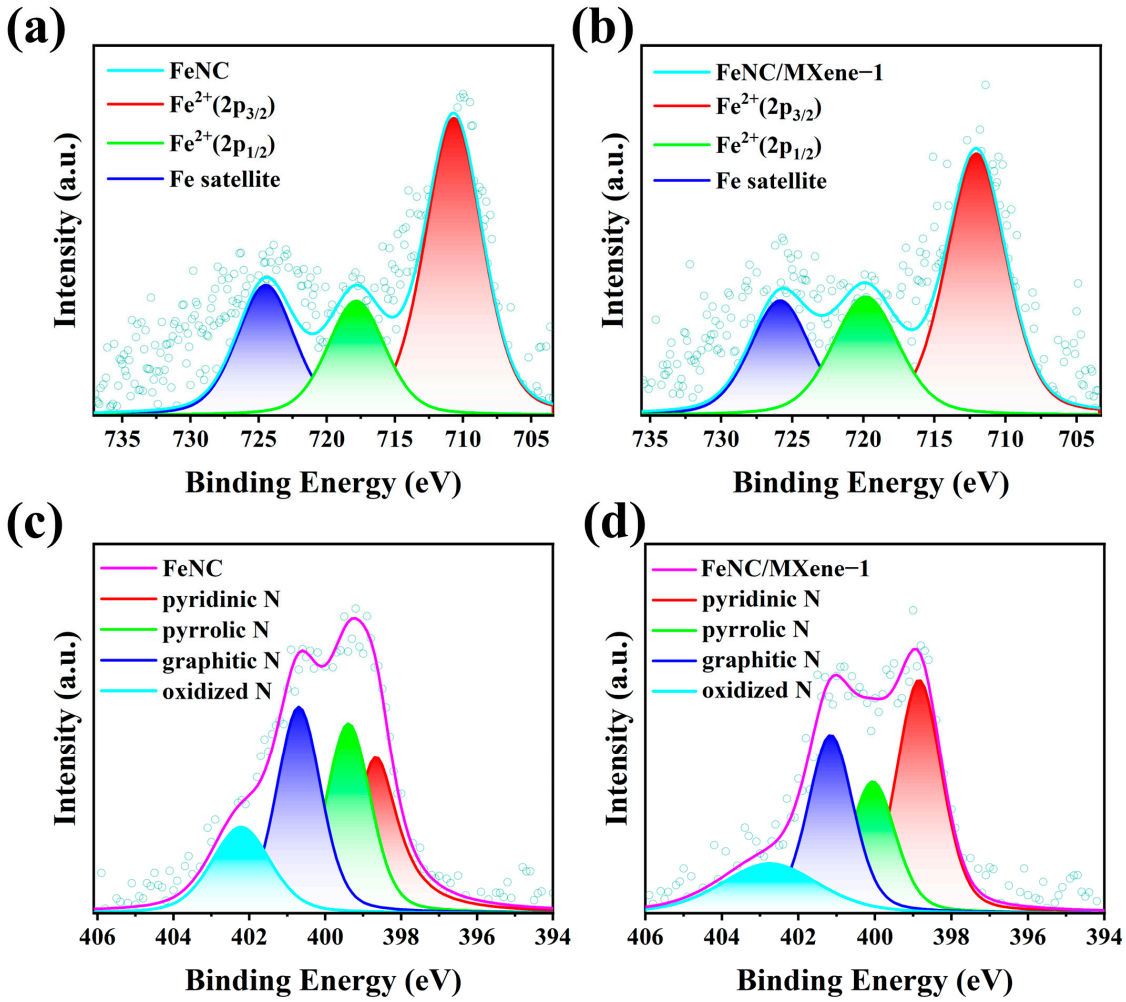


Figure 4. (**a**–**d**) XPS survey spectra and (**a**) high-resolution Fe2p scans of FeNC. (**b**) High-resolution Fe2p scan of FeNC/MXene-1. (**c**) High-resolution N1s scans of FeNC. (**d**) High-resolution N1s scans of FeNC/MXene-1.

Additionally, as depicted in Figure 4c, the N1s spectrum was fitted into four main N-related peaks along with supplementary MXene-N bonds, corresponding to pyridinic N, pyrrolic N, graphitic N, and oxidized N, which are observed at 400.5 eV, 399.4 eV, 398.3 eV, and 402.7 eV, respectively. As can be observed in Table 1, the proportions of pyridinic N, pyrrolic N, and graphitic N in FeNC/MXene are 31.95%, 25.15%, and 21.94%, respectively. The pyridinic N is connected to two carbon atoms and contributes two p-electrons to the aromatic system, while the graphitic N is bonded to three carbon atoms. The pyrrolic N-substituted nitrogen atom is bonded to two carbon atoms at the edge of the carbon plane and donates one p-electron, whereas the oxidized N-substituted nitrogen atom is bonded to two carbon atoms and one oxygen atom [50]. The four types of nitrogen species exhibit different effects on the ORR activity of the electrocatalyst, with pyridinic N showing the strongest contribution. It enhances electron-donating capability and facilitates O_2 adsorption, thereby improving catalytic performance. Notably, the enhanced ORR activity is primarily attributed to this effect [51]. Graphitic N provides a substantial number of

electrocatalytic active centers for the ORR, thereby enhancing the limiting current density. Additionally, pyrrolic N sites contribute to improved ORR performance, although their impact on overall catalyst performance is minimal [52]. As shown in Table 1, the increase in the pyridinic N content of the FeNC/MXene catalysts indicates that the catalysts have improved limiting current densities and onset potentials (E_{onset}) toward ORR.

Table 1. Deconvoluted N1s atomic percentage of FeNC and FeNC/MXene-1.

Catalysts	Pyridinic N	Pyrrolic N	Graphite N	Oxygen N
FeNC	27.12%	27.15	29.56%	16.17%
FeNC/MXene-1	36.08%	20.29%	27.66%	15.97%

3.2. Electrochemical Properties of FeNC/MXene

The ORR performance of the synthesized catalyst FeNC/MXene was analyzed in an alkaline electrolyte (0.1 M KOH) with the rotating disk electrode (RDE) method. Initially, the electrocatalytic behavior of the catalyst was assessed in an electrolyte saturated with O_2 and N_2 through cyclic voltammetry (CV) cycling at a scan rate of 10 mV s^{-1}. As illustrated in Figure 5a, the absence of a redox peak in the N_2-saturated electrolyte supports the assertion that the electrocatalyst exhibits capacitive behavior [53]. Conversely, the O_2-saturated electrolyte exhibited a cathodic redox peak at a potential of 0.85 V for FeNC/MXene. A series of catalysts, designated as FeNC/MXene-1, FeNC/MXene-2, FeNC/MXene-3, and FeNC/MXene-4, were synthesized by adjusting the ratios of FeNC to MXene to 1:1, 1:2, 1:3, and 2:1, respectively. Subsequently, the ORR catalytic activity of these catalysts was compared with that of commercial Pt/C using linear sweep voltammetry (LSV). As shown in Figure 5b, single FeNC exhibits discernible ORR activity. The electrochemical activity of FeNC is altered when loaded on MXene, particularly at a 1:1 ratio, which demonstrates a significant enhancement in ORR activity. As shown in Figure 5c, a detailed comparison of the onset potential, half-wave potential, and limiting current density was conducted for the different catalysts. The FeNC/MXene-1 catalyst exhibits an onset potential of 0.987 V, comparable to that of commercial Pt/C (0.997 V), and a half-wave potential of 0.857 V, which even surpasses that of Pt/C (0.845 V). Moreover, compared to FeNC, FeNC/MXene-1 shows a significantly enhanced limiting current density, reaching 5.5 mA cm^{-2}. This is attributed to the synergistic combination of conductive Vulcan XC-72, the layered structure of MXene with high electronic conductivity, and the graphitized carbon surrounding Fe-N_x sites, which together provide efficient electron transfer pathways. These characteristics facilitate rapid charge transfer and mass diffusion. As shown in Figure S3, the ORR performance of the MXene substrate and metal-free N-C was evaluated using LSV. The MXene substrate exhibited minimal ORR activity due to the absence of active sites. Metal-free N-C showed moderate activity, attributed to the presence of pyridinic nitrogen. However, both materials displayed significantly lower ORR performance compared to the FeNC/MXene catalyst, highlighting the critical role of Fe-N_x sites in enhancing catalytic activity. The ORR kinetics of all samples were assessed using the Tafel slope, as shown in Figure 5d. The Tafel slope of the FeNC/MXene-1, measured at 67 mV dec^{-1}, is smaller than that of Pt/C (90 mV dec^{-1}) and FeNC (72 mV dec^{-1}), suggesting more favorable -oxygen reduction kinetics. These results indicate that the FeNC/MXene-1 catalyst exhibits superior ORR activity, likely due to its high concentration of FeN_x sites and its layered structure [54]. The ORR performance of FeNC/MXene was compared with other reported Fe-based catalysts (see Table S1 [55–64]). The results indicate that FeNC/MXene shows ORR performance similar to other Fe-based catalysts. To further examine the ORR kinetics, the catalysts were tested in a 0.1 M KOH O_2-saturated electrolyte using an LSV system at a scan rate of 10 mV s^{-1} and rotation speeds between 400 and 1600 rpm. As seen in Figure 5e,

the limiting current density increases with the rotation speed [65]. The corresponding K-L plot, illustrated in Figure 5f, is nearly linear in three dimensions within the 0.1 mol L^{-1} KOH solution, confirming first-order reaction kinetics. Through the K-L equation, the value of n for the FeNC/MXene-1 catalyst is calculated to be around 4.0 within the potential range of 0.2 V–0.6 V, suggesting a direct four-electron transfer pathway for the ORR [66].

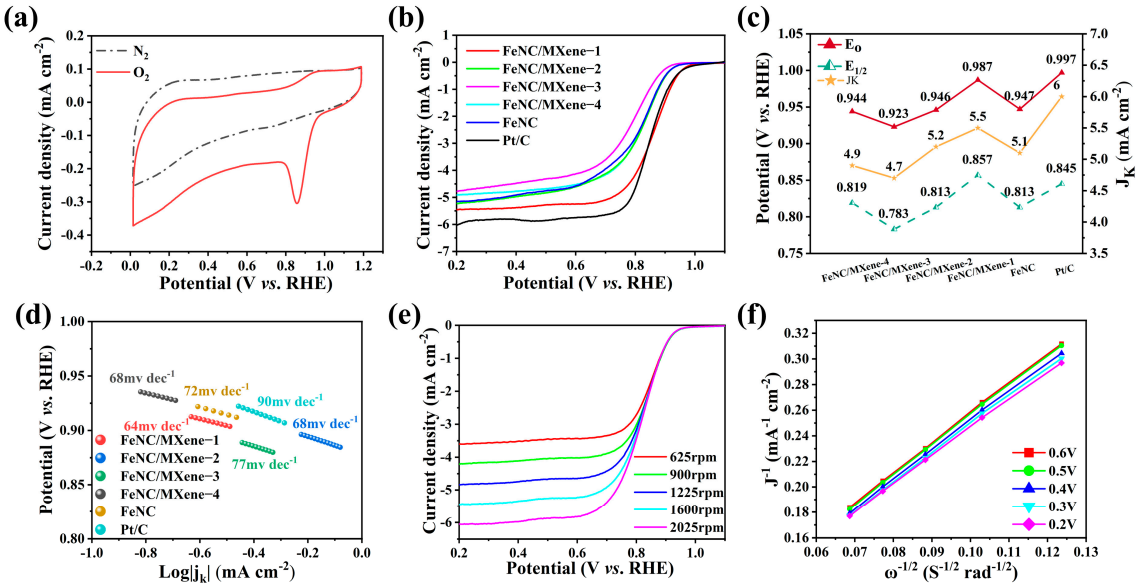


Figure 5. (**a**) CV curves of FeNC/MXene-1, (**b**) LSV curves of FeNC/MXene-1, FeNC/MXene-2, FeNC/MXene-3, FeNC/MXene-4, and Pt/C at 1600 rpm, (**c**) the corresponding E_{onset}, $E_{1/2}$, and J_k, (**d**) Tafel slope of the above catalyst, (**e**) LSV curves of FeNC/MXene-1 at various rotation speeds of the RDE, and (**f**) Koutecky-Levich (K-L) curves of FeNC/MXene-1 at various potentials.

The LSV test reveals that the FeNC/MXene composite at a 1:1 ratio exhibits the highest ORR activity in alkaline electrolytes, thereby establishing this ratio as optimal. Catalysts synthesized at this ratio, differentiated by distinct pyrolysis temperatures, are designated as FeNC/MXene-700, FeNC/MXene-800 (FeNC/MXene-1), and FeNC/MXene-900. The ORR performance of these catalysts was assessed through cyclic voltammetry (CV) curves under saturated nitrogen (N_2) and oxygen (O_2) conditions in a 0.1 mol L^{-1} KOH electrolyte. In the alkaline solution saturated with N_2, none of the catalysts displayed a cathodic ORR peak. In contrast, under O_2 saturation, a cathodic oxygen reduction peak was identified at a potential of 0.82 V for FeNC/MXene-700 (Figure S4a), while FeNC/MXene-900 demonstrated a peak at a slightly lower potential of 0.80 V (Figure S4b). The findings indicate that the FeNC/MXene-800 composite achieves the most positive ORR peak potential, suggesting an enhanced likelihood of O_2 reduction to H_2O [67].

Additionally, the ORR performance of the catalysts in the O_2-saturated 0.1 M KOH electrolyte at various pyrolysis temperatures was recorded via LSV at a scan rate of 10 mV s^{-1} and a rotation speed of 1600 rpm. As shown in Figure 6a, the onset potential (E_{onset}) and half-wave potential ($E_{1/2}$) for FeNC/MXene-700 are 0.933 V and 0.812 V, respectively, whereas those for FeNC/MXene-900 are 0.905 V and 0.778 V. These results are comparatively lower than those of FeNC/MXene-1. This indicates that maintaining a 1:1 mass ratio and performing pyrolysis at 800 °C effectively enhance the loading of FeNC onto the MXene substrate. Furthermore, the ORR kinetics of all samples were assessed using the Tafel slope, as shown in Figure 6b. The Tafel slope of FeNC/MXene-800 is lower than that of other pyrolysis temperatures, indicating better reaction kinetics. This enhancement arises from the conversion of MXene at pyrolysis temperatures of 800 °C, which results in a beneficial synergistic effect due to the coexistence of rutile and anatase TiO_2. This effect

significantly improves the mass transfer rate and electrical conductivity of the catalytic layer [42,43].

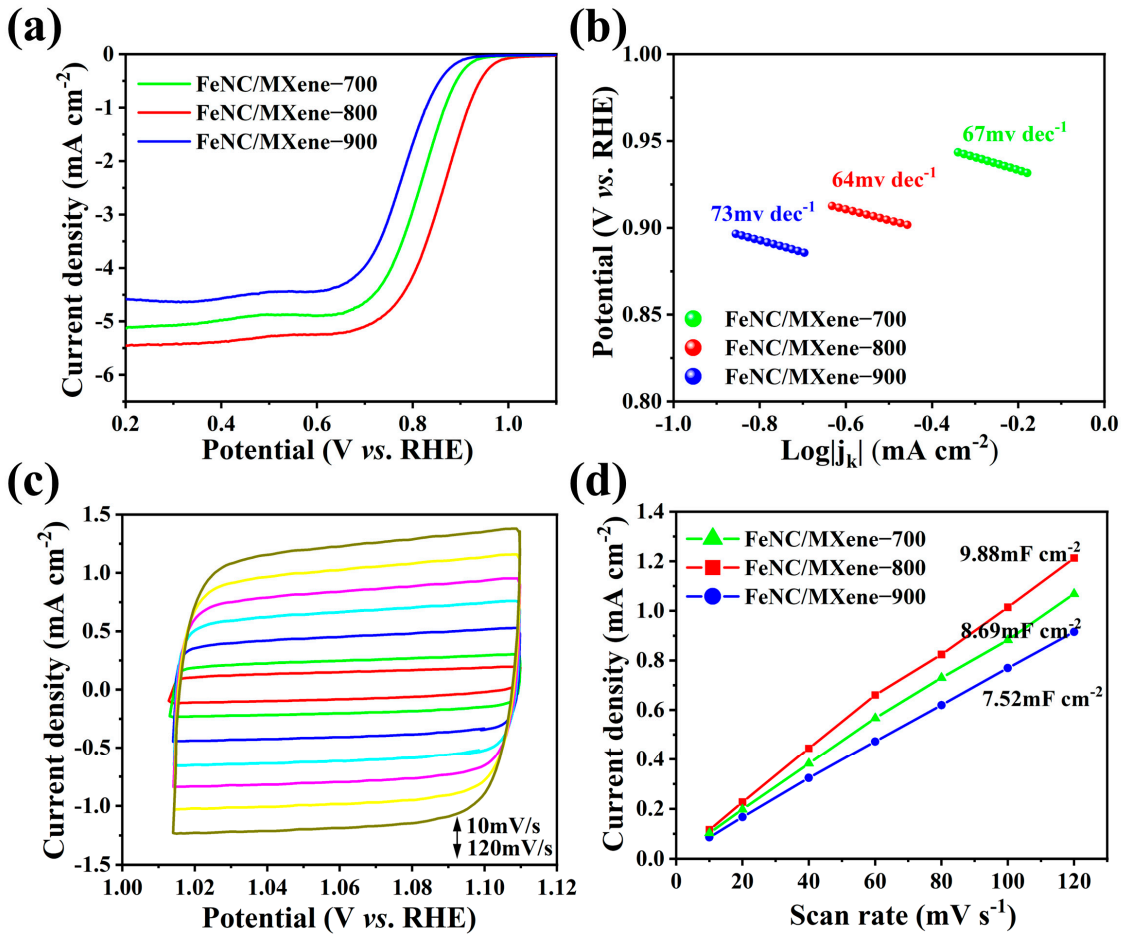


Figure 6. (**a**,**b**) The LSV curves and Tafel slope of FeNC/MXene-1 at various temperatures, (**c**) the ECSA curves of FeNC/MXene-1 at CV scan rates ranging from 10 mV s^{-1} to 120 mV s^{-1} (The different colors represent the corresponding scan rates), (**d**) the direct correlation between the recorded capacitive current and different scanning speeds.

The electrochemical surface area (ECSA) plays an important role in influencing electrocatalytic performance for the ORR. The ECSA was determined from the electrochemical double-layer capacitance (C_{dl}) measured during the CV cycling of the obtained electrocatalysts, namely, FeNC/MXene-700, FeNC/MXene-800, and FeNC/MXene-900, at different scan rates between 10 mV s^{-1} and 120 mV s^{-1} (see Figures 6c and S4c,d). The C_{dl} values were determined using the following equation:

$$\Delta j = j_a - j_c$$

$$C_{dl} = d(\Delta j)/2d\nu$$

$$ECSA = C_{dl}/C_s$$

here, j_a and j_c denote the currents measured at the anode and cathode during cyclic voltammetry in mA cm^{-2}, Δj refers to the current difference between the anode and cathode, and C_s represents the specific capacitance of the planar electrode, with units of μF cm^{-2}. The C_s value for non-precious metals typically ranges from 20 to 40 μF cm^{-2}. In this study, an average value of 40 μF cm^{-2} was used. The capacitance per unit area (C_{dl}) of FeNC/MXene-700, FeNC/MXene-800, and FeNC/MXene-900, as shown in Figure 6d, is

8.69 μF cm^{-2}, 9.88 μF cm^{-2}, and 7.52 μF cm^{-2}, respectively. The highest calculated ECSA was 247 m^2 g^{-1} for FeNC/MXene-800, followed by FeNC/MXene-700 (217 m^2 g^{-1}) and FeNC/MXene-900 (188 m^2 g^{-1}). These ECSA results align with the LSV measurements of the synthetic catalysts. As the pyrolysis temperature increases, Vulcan XC72 gradually eliminates the oxygen-containing functional groups on its surface, which enhances the electrical conductivity and hydrophobicity of the carbon material. At a pyrolysis temperature of 800 °C, the microporous structure of Vulcan XC72 significantly enhances the utilization efficiency of the MXene layer. When the pyrolysis temperature reaches 900 °C, the arrangement of the carbon layers begins to graphitize; however, at elevated temperatures, the micropores collapse, resulting in a decrease in specific surface area [68]. These ECSA results correlate well with the LSV measurements of the synthesized catalysts.

3.3. Stability and Durability of FeNC/MXene

In the context of actual operating conditions for a hydrogen fuel cell, a number of factors contribute to catalyst degradation. These include carbon corrosion, metal peeling, the protonation of active centers, and intermediate formation [69,70]. The durability of FeNC/MXene-1 and commercial Pt/C was evaluated through chronoamperometry, as depicted in Figure 7a. The FeNC/MXene-1 catalyst exhibited excellent stability, maintaining a current loss of only 9% after 20,000 s of operation at 0.6 V. This is a notable improvement over the current loss rate of 25% observed for the Pt/C catalyst. Apart from its stable performance, the FeNC/MXene-1 catalyst demonstrated remarkable methanol tolerance, retaining 91% of its initial current density after 1500 s of testing in the presence of 3M methanol (CH_3OH) for 300 s (see Figure 7b). In contrast, the commercial Pt/C catalyst exhibited a 29% reduction in current density. As conventional metals are inherently less tolerant of methanol interference, the good resistance to toxicity of FeNC/MXene can be attributed to the rich microporous carbon structure of Vulcan XC72, which enhances the smooth diffusion rate of the electrolyte. The experimental results demonstrate that FeNC/MXene-1 exhibits excellent methanol poisoning resistance and long-term cycling stability. The FeNC/MXene-1 catalyst has the potential to be a low-cost ORR electrocatalyst for the circular economy and sustainable hydrogen-fueled fuel cells and direct methanol fuel cells.

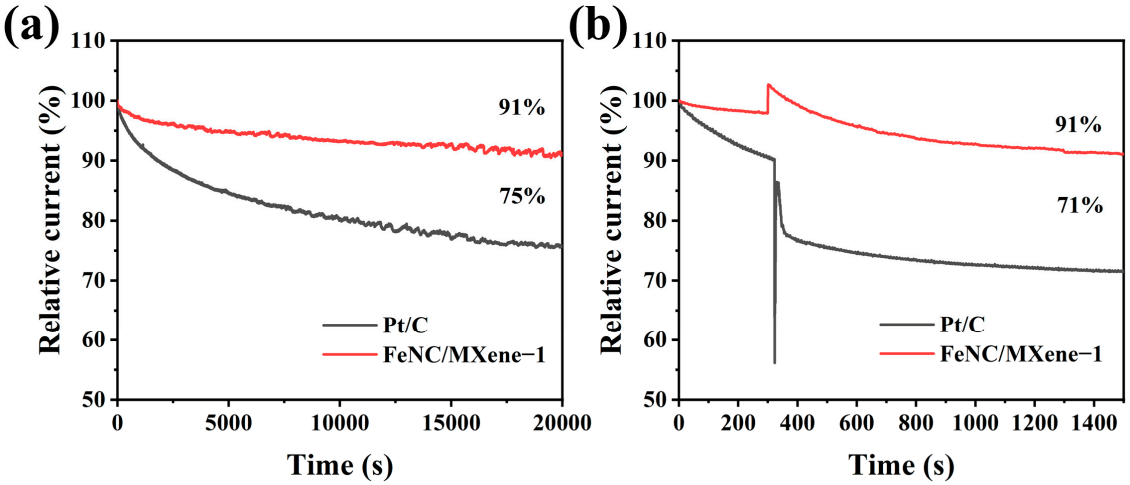


Figure 7. (**a**) Chronoamperometry curves of FeNC/MXene-1 and Pt/C were recorded at a constant potential of 0.6 V (vs. RHE) over a duration of 20,000 s. (**b**) Chronoamperometry curves of FeNC/MXene-1 and Pt/C at a constant voltage of 0.6 V (vs. RHE) for 1500 s after the addition of methanol.

4. Conclusions

In conclusion, oxygen reduction reaction activity was enhanced by anchoring iron–nitrogen–carbon (Fe-N_x-C) complexes on a Ti_3C_2-based MXene substrate. SEM and TEM analyses show that FeNC particles are uniformly dispersed across both the surface and interlayer of the MXene. XPS results reveal an increase in pyridine nitrogen concentration, which improves the catalyst's performance. In a 0.1 M KOH electrolyte, the FeNC/MXene catalyst exhibits a half-wave potential of 0.857 V, surpassing the 0.845 V of Pt/C catalysts. Additionally, the FeNC/MXene materials demonstrate excellent durability and methanol resistance compared to commercial Pt/C catalysts. The high catalytic activity and stability of FeNC/MXene provide a valuable reference for developing non-precious metal ORR catalysts and expanding the use of Pt/C in alternative fuel cells.

Supplementary Materials: The following supporting information can be downloaded at https://www.mdpi.com/article/10.3390/inorganics13060188/s1, Figure S1: SEM of MAX; Figure S2: XPS survey spectra of FeNC/MXene-1; Figure S3: LSV curves of MXene and metal-free N-C at 1600 rpm; Figure S4: (a,b) CV curves of FeNC/Mene-700 and FeNC/Mene-900, (c,d) ECSA curves at different CV scan rate of 10 mV/s to 120 mV/s of FeNC/Mene-700 and FeNC/Mene-900. Table S1: Performance comparison of ORR activities for recently reported Fe-based catalysts. References [55–64] are cited in the supplementary materials.

Author Contributions: Conceptualization, H.Z.; Methodology, H.Z.; Software, H.Z.; Validation, H.Z.; Formal analysis, F.W. and W.S.; Investigation, H.Z.; Data curation, F.W.; Writing—original draft, H.Z.; Writing—review & editing, F.W. and W.S.; Supervision, F.W.; Project administration, W.S.; Funding acquisition, F.W. All authors have read and agreed to the published version of the manuscript.

Funding: This work was supported by the Natural Science Foundation of Shandong Province (ZR2020ME041, ZR2022QB173, ZR2023MB054), Joint Zibo-SDUT Fund (2019ZBXC358), and the Foundation of State Key Laboratory of Biobased Material and Green Papermaking, Qilu University of Technology (Shandong Academy of Sciences) (KF2019-06).

Institutional Review Board Statement: Not applicable.

Informed Consent Statement: Not applicable.

Data Availability Statement: All data generated or analyzed during this study are included in this published article and its ESI.

Conflicts of Interest: The authors declare that they have no known competing financial interests or personal relationships that could have appeared to influence the work reported in this paper.

References

1. Li, Z.; He, H.; Cao, H.; Sun, S.; Diao, W.; Gao, D.; Lu, P.; Zhang, S.; Guo, Z.; Li, M.; et al. Atomic Co/Ni dual sites and Co/Ni alloy nanoparticles in N-doped porous Janus-like carbon frameworks for bifunctional oxygen electrocatalysis. *Appl. Catal. B Environ.* **2019**, *240*, 112–121. [CrossRef]
2. Eftekhari, A.; Fang, B. Electrochemical hydrogen storage: Opportunities for fuel storage, batteries, fuel cells, and supercapacitors. *Int. J. Hydrogen Energy* **2017**, *42*, 25143–25165. [CrossRef]
3. Wang, X.; Yu, M.; Feng, X. Electronic structure regulation of noble metal-free materials toward alkaline oxygen electrocatalysis. *eScience* **2023**, *3*, 100141. [CrossRef]
4. Yang, X.; Lin, L.; Guo, X.; Zhang, S. Design of Multifunctional Electrocatalysts for ORR/OER/HER/HOR: Janus Makes Difference. *Small* **2024**, *20*, e2404000. [CrossRef]
5. Yang, Y.; Li, P.; Zheng, X.; Sun, W.; Dou, S.X.; Ma, T.; Pan, H. Anion-exchange membrane water electrolyzers and fuel cells. *Chem. Soc. Rev.* **2022**, *51*, 9620–9693. [CrossRef]
6. Zeng, Q.; Chang, S.; Wang, M.; Li, M.; Deng, Q.; Xiong, Z.; Zhou, B.; Liu, Y. Highly-active, metal-free, carbon-based ORR cathode for efficient organics removal and electricity generation in a PFC system. *Chin. Chem. Lett.* **2021**, *32*, 2212–2216. [CrossRef]
7. Bhoyate, S.D.; Kim, J.; de Souza, F.M.; Lin, J.; Lee, E.; Kumar, A.; Gupta, R.K. Science and engineering for non-noble-metal-based electrocatalysts to boost their ORR performance: A critical review. *Coord. Chem. Rev.* **2023**, *474*, 214854. [CrossRef]

8. Chen, D.; Yuan, J.; Zhang, J.; Li, G.; Tian, L.; Wang, Z.; Hu, J.; Zhang, Y.; Li, C.; Yu, J.; et al. Construction of atom-scale Co/Fe/Ni M-N-C active sites within nitrogen-doped carbon spheres for high-performance bifunctional oxygen catalysts in rechargeable zinc-air batteries. *J. Energy Storage* **2024**, *101*, 113772. [CrossRef]
9. Ye, C.; Zhang, L.; Shen, Y. Activity Origin and Catalytic Mechanism of the M–N–C Catalysts for the Oxygen Reduction Reaction. *ACS Mater. Lett.* **2024**, *6*, 2858–2887. [CrossRef]
10. Liu, J.; Wan, X.; Liu, S.; Liu, X.; Zheng, L.; Yu, R.; Shui, J. Hydrogen Passivation of M–N–C (M = Fe, Co) Catalysts for Storage Stability and ORR Activity Improvements. *Adv. Mater.* **2021**, *33*, e2103600. [CrossRef]
11. Li, X.; Wang, D.; Zha, S.; Chu, Y.; Pan, L.; Wu, M.; Liu, C.; Wang, W.; Mitsuzaki, N.; Chen, Z. Active sites identification and engineering of M-N-C electrocatalysts toward oxygen reduction reaction. *Int. J. Hydrogen Energy* **2024**, *51*, 1110–1127. [CrossRef]
12. Liu, H.; Zhou, Y.; Zhu, S.; Zheng, L.; Cui, Z.; Li, Z.; Wu, S.; Ma, L.; Liang, Y. Highly durable Cu–N–C active sites towards efficient oxygen reduction for zinc-air battery: Carbon matrix effect, reaction mechanism and pathways. *J. Alloys Compd.* **2021**, *857*, 158321. [CrossRef]
13. Zhao, X.; Liu, X.; Huang, B.; Wang, P.; Pei, Y. Hydroxyl group modification improves the electrocatalytic ORR and OER activity of graphene supported single and bi-metal atomic catalysts (Ni, Co, and Fe). *J. Mater. Chem. A* **2019**, *7*, 24583–24593. [CrossRef]
14. Wan, X.; Liu, Q.; Liu, J.; Liu, S.; Liu, X.; Zheng, L.; Shang, J.; Yu, R.; Shui, J. Iron atom–cluster interactions increase activity and improve durability in Fe–N–C fuel cells. *Nat. Commun.* **2022**, *13*, 2963. [CrossRef]
15. Dong, X.; Wang, J.; Wang, X.; Xu, J.; Yang, J.; Zeng, W.; Zhang, Y.; Huang, G.; Wang, J.; Pan, F. Prussian Blue Analogue-Derived Bimetallic CoFe@NC as Effective and Extremely Stable Oxygen Reduction Electrocatalysts for Mg-Air Battery. *ACS Appl. Energy Mater.* **2022**, *5*, 12272–12282. [CrossRef]
16. Guo, S.; Lian, J.; Zhao, J.; Zhang, Y.; Wang, X. Se Atom Doping Enhances the Catalytic Activity of Co@NC for Oxygen Reduction Reaction. *Energy Technol.* **2023**, *11*, 2300205. [CrossRef]
17. Wang, H.; Cao, L.; Feng, Y.; Chen, J.; Feng, W.; Luo, T.; Hu, Y.; Yuan, C.; Zhao, Y.; Zhao, Y.; et al. Facile synthesis of defect-rich Fe-N-C hybrid from fullerene/ferrotetraphenylporphyrin as efficient oxygen reduction electrocatalyst for Zn-air battery. *Chin. Chem. Lett.* **2023**, *34*, 107601. [CrossRef]
18. Zhang, F.; Liu, X.; Chen, Y.; Tian, M.; Yang, T.; Zhang, J.; Gao, S. Ordered mesoporous carbon fiber bundles with high-density and accessible Fe-NX active sites as efficient ORR catalysts for Zn-air batteries. *Chin. Chem. Lett.* **2023**, *34*, 108142. [CrossRef]
19. Liu, K.; Fu, J.; Luo, T.; Ni, G.; Li, H.; Zhu, L.; Wang, Y.; Lin, Z.; Sun, Y.; Cortés, E.; et al. Potential-Dependent Active Moiety of Fe–N–C Catalysts for the Oxygen Reduction Reaction. *J. Phys. Chem. Lett.* **2023**, *14*, 3749–3756. [CrossRef] [PubMed]
20. Qiu, X.; Wang, Y.; Shao, M. High-performance and durable Fe–N–C fuel cell catalysts. *Joule* **2024**, *8*, 881–882. [CrossRef]
21. Zhou, Y.; Lu, R.; Tao, X.; Qiu, Z.; Chen, G.; Yang, J.; Zhao, Y.; Feng, X.; Müllen, K. Boosting Oxygen Electrocatalytic Activity of Fe–N–C Catalysts by Phosphorus Incorporation. *J. Am. Chem. Soc.* **2023**, *145*, 3647–3655. [CrossRef]
22. Ma, Q.; Jin, H.; Zhu, J.; Li, Z.; Xu, H.; Liu, B.; Zhang, Z.; Ma, J.; Mu, S. Stabilizing Fe–N–C Catalysts as Model for Oxygen Reduction Reaction. *Adv. Sci.* **2021**, *8*, e2102209. [CrossRef]
23. Qin, G.; Sun, S.; Zhang, X.; Han, Z.; Li, Y.; Han, G.; Li, Y.; Zhu, S. Millisecond activity modulation of atomically-dispersed Fe–N–C catalysts. *Energy Storage Mater.* **2024**, *69*, 103421. [CrossRef]
24. Peng, P.; Shi, L.; Huo, F.; Mi, C.; Wu, X.; Zhang, S.; Xiang, Z. A pyrolysis-free path toward superiorly catalytic nitrogen-coordinated single atom. *Sci. Adv.* **2019**, *5*, eaaw2322. [CrossRef]
25. Wang, T.; Sun, C.; Yan, Y.; Li, F. Understanding the active sites of Fe–N–C materials and their properties in the ORR catalysis system. *RSC Adv.* **2022**, *12*, 9543–9549. [CrossRef]
26. Ahmad Junaidi, N.H.; Wong, W.Y.; Loh, K.S.; Rahman, S.; Choo, T.F.; Wu, B. Enhanced oxygen reduction reaction catalyst stability and durability of MXene-supported Fe-N-C catalyst for proton exchange membrane fuel cell application. *J. Alloys Compd.* **2023**, *968*, 171898. [CrossRef]
27. Gu, W.; Wu, M.; Xu, J.; Zhao, T. MXene boosted metal-organic framework-derived Fe–N–C as an efficient electrocatalyst for oxygen reduction reactions. *Int. J. Hydrogen Energy* **2022**, *47*, 17224–17232. [CrossRef]
28. Lisheshar, I.W.; Rouhi, S.; Ay, F.; Kosku Perkgöz, N. High-performance supercapacitors based on nonfunctionalized MXenes. *J. Power Sources* **2025**, *628*, 235894. [CrossRef]
29. Wu, M.; Fan, X.; Zhang, W.; Chen, B.; Ye, T.; Zhang, Q.; Fang, Y.; Wang, Y.; Tang, Y. Highly dispersed Ru nanospecies on N-doped carbon/MXene composite for highly efficient alkaline hydrogen evolution. *Chin. Chem. Lett.* **2024**, *35*, 109258. [CrossRef]
30. Cheng, H.; Liu, Y.; Cheng, Z.; Wang, X.; Huang, N.; Zhang, H. Ti3C2Tx MXene wrapped, carbon-coated porous Si sheets for improved lithium storage performance. *Chin. Chem. Lett.* **2024**, *35*, 108923. [CrossRef]
31. Tyagi, N.; Bhardwaj, V.; Moka, S.; Singh, M.K.; Khanuja, M.; Sharma, G. An overview on synthesis of MXene and MXene based nanocomposites for supercapacitors. *Mater. Today Commun.* **2024**, *41*, 110223. [CrossRef]
32. Zhao, L.; Dong, B.; Li, S.; Zhou, L.; Lai, L.; Wang, Z.; Zhao, S.; Han, M.; Gao, K.; Lu, M.; et al. Interdiffusion Reaction-Assisted Hybridization of Two-Dimensional Metal–Organic Frameworks and Ti3C2Tx Nanosheets for Electrocatalytic Oxygen Evolution. *ACS Nano* **2017**, *11*, 5800–5807. [CrossRef]

33. Ran, J.; Gao, G.; Li, F.-T.; Ma, T.-Y.; Du, A.; Qiao, S.-Z. Ti3C2 MXene co-catalyst on metal sulfide photo-absorbers for enhanced visible-light photocatalytic hydrogen production. *Nat. Commun.* **2017**, *8*, 13907. [CrossRef]
34. Peng, X.; Zhao, S.; Mi, Y.; Han, L.; Liu, X.; Qi, D.; Sun, J.; Liu, Y.; Bao, H.; Zhuo, L.; et al. Trifunctional Single-Atomic Ru Sites Enable Efficient Overall Water Splitting and Oxygen Reduction in Acidic Media. *Small* **2020**, *16*, e2002888. [CrossRef]
35. Li, Z.; Zhuang, Z.; Lv, F.; Zhu, H.; Zhou, L.; Luo, M.; Zhu, J.; Lang, Z.; Feng, S.; Chen, W.; et al. The Marriage of the FeN4 Moiety and MXene Boosts Oxygen Reduction Catalysis: Fe 3d Electron Delocalization Matters. *Adv. Mater.* **2018**, *30*, e1803220. [CrossRef]
36. Alhabeb, M.; Maleski, K.; Anasori, B.; Lelyukh, P.; Clark, L.; Sin, S.; Gogotsi, Y. Guidelines for Synthesis and Processing of Two-Dimensional Titanium Carbide ($Ti_3C_2T_x$ MXene). *Chem. Mater.* **2017**, *29*, 7633–7644. [CrossRef]
37. Mahmood, M.; Rasheed, A.; Ayman, I.; Rasheed, T.; Munir, S.; Ajmal, S.; Agboola, P.O.; Warsi, M.F.; Shahid, M. Synthesis of Ultrathin MnO_2 Nanowire-Intercalated 2D-MXenes for High-Performance Hybrid Supercapacitors. *Energy Fuels* **2021**, *35*, 3469–3478. [CrossRef]
38. Pinheiro, V.S.; Paz, E.C.; Aveiro, L.R.; Parreira, L.S.; Souza, F.M.; Camargo, P.H.C.; Santos, M.C. Ceria high aspect ratio nanostructures supported on carbon for hydrogen peroxide electrogeneration. *Electrochim. Acta* **2018**, *259*, 865–872. [CrossRef]
39. Sabry, R.S.; Al-Haidarie, Y.K.; Kudhier, M.A. Synthesis and photocatalytic activity of TiO2 nanoparticles prepared by sol–gel method. *J. Sol-Gel Sci. Technol.* **2016**, *78*, 299–306. [CrossRef]
40. Muhyuddin, M.; Berretti, E.; Mirshokraee, S.A.; Orsilli, J.; Lorenzi, R.; Capozzoli, L.; D'Acapito, F.; Murphy, E.; Guo, S.; Atanassov, P.; et al. Formation of the active site structures during pyrolysis transformation of Fe-phthalocyanine into Fe-Nx-C electrocatalysts for the oxygen reduction reaction. *Appl. Catal. B Environ.* **2024**, *343*, 123515. [CrossRef]
41. Zhang, J.; Zhang, X.; Yue, W. Boosting electrocatalytic oxygen reduction performance of CoNC catalysts on Ti_3C_2 MXene by the synergistic effect with oxygen vacancy-rich TiO_2. *Chem. Eng. J.* **2023**, *456*, 141101. [CrossRef]
42. Li, J.; Zhou, H.; Zhuo, H.; Wei, Z.; Zhuang, G.; Zhong, X.; Deng, S.; Li, X.; Wang, J. Oxygen vacancies on TiO_2 promoted the activity and stability of supported Pd nanoparticles for the oxygen reduction reaction. *J. Mater. Chem. A* **2018**, *6*, 2264–2272. [CrossRef]
43. Pei, D.-N.; Gong, L.; Zhang, A.-Y.; Zhang, X.; Chen, J.-J.; Mu, Y.; Yu, H.-Q. Defective titanium dioxide single crystals exposed by high-energy {001} facets for efficient oxygen reduction. *Nat. Commun.* **2015**, *6*, 8696. [CrossRef]
44. Shi, F.; Baker, L.R.; Hervier, A.; Somorjai, G.A.; Komvopoulos, K. Tuning the Electronic Structure of Titanium Oxide Support to Enhance the Electrochemical Activity of Platinum Nanoparticles. *Nano Lett.* **2013**, *13*, 4469–4474. [CrossRef]
45. Xie, X.; Zhao, M.-Q.; Anasori, B.; Maleski, K.; Ren, C.E.; Li, J.; Byles, B.W.; Pomerantseva, E.; Wang, G.; Gogotsi, Y. Porous heterostructured MXene/carbon nanotube composite paper with high volumetric capacity for sodium-based energy storage devices. *Nano Energy* **2016**, *26*, 513–523. [CrossRef]
46. Yu, L.; Hu, L.; Anasori, B.; Liu, Y.-T.; Zhu, Q.; Zhang, P.; Gogotsi, Y.; Xu, B. MXene-Bonded Activated Carbon as a Flexible Electrode for High-Performance Supercapacitors. *ACS Energy Lett.* **2018**, *3*, 1597–1603. [CrossRef]
47. Li, X.; Chen, Y.; Zhao, Z.; Huang, Y.; Zhu, K.; Feng, S.; Luo, S.; Wang, L.; Yan, K. A single-atom Fe–N_2 embedded in nitrogen-doped porous carbon as a bifunctional photocatalyst for efficient removal of marine petroleum pollutants. *Environ. Funct. Mater.* **2023**, *2*, 66–75. [CrossRef]
48. Chang, K.; Chen, W. Single-layer MoS_2/graphene dispersed in amorphous carbon: Towards high electrochemical performances in rechargeable lithium ion batteries. *J. Mater. Chem.* **2011**, *21*, 17175–17184. [CrossRef]
49. Zhao, L.; Zhang, Y.; Huang, L.-B.; Liu, X.-Z.; Zhang, Q.-H.; He, C.; Wu, Z.-Y.; Zhang, L.-J.; Wu, J.; Yang, W.; et al. Cascade anchoring strategy for general mass production of high-loading single-atomic metal-nitrogen catalysts. *Nat. Commun.* **2019**, *10*, 1278. [CrossRef] [PubMed]
50. Kaur, P.; Verma, G.; Sekhon, S.S. Biomass derived hierarchical porous carbon materials as oxygen reduction reaction electrocatalysts in fuel cells. *Prog. Mater. Sci.* **2019**, *102*, 1–71. [CrossRef]
51. Nie, Y.; Xie, X.; Chen, S.; Ding, W.; Qi, X.; Wang, Y.; Wang, J.; Li, W.; Wei, Z.; Shao, M. Towards Effective Utilization of Nitrogen-Containing Active Sites: Nitrogen-doped Carbon Layers Wrapped CNTs Electrocatalysts for Superior Oxygen Reduction. *Electrochim. Acta* **2016**, *187*, 153–160. [CrossRef]
52. Bao, X.; Nie, X.; von Deak, D.; Biddinger, E.J.; Luo, W.; Asthagiri, A.; Ozkan, U.S.; Hadad, C.M. A First-Principles Study of the Role of Quaternary-N Doping on the Oxygen Reduction Reaction Activity and Selectivity of Graphene Edge Sites. *Top. Catal.* **2013**, *56*, 1623–1633. [CrossRef]
53. Bera, B.; Chakraborty, A.; Kar, T.; Leuaa, P.; Neergat, M. Density of States, Carrier Concentration, and Flat Band Potential Derived from Electrochemical Impedance Measurements of N-Doped Carbon and Their Influence on Electrocatalysis of Oxygen Reduction Reaction. *J. Phys. Chem. C* **2017**, *121*, 20850–20856. [CrossRef]
54. Cao, L.; Zhang, M.; Su, K.; Gu, F.; Li, Z. Fe–Nx–C sites decorated porous carbon nanorods with huge specific surface area boost oxygen reduction catalysis for Zn-air batteries. *J. Alloys Compd.* **2021**, *868*, 159015. [CrossRef]

55. Chen, L.; Wang, X.; Lu, T.; Pang, H.; Zhang, S.; Xu, L.; Yang, G.; Zhou, Q.; Tang, Y. Maneuver of the d-Orbital Spin Polarization of Fe Single Atomic Sites via a Near-Range Axial Ligand Effect for Boosting Oxygen Reduction Reaction. *Appl. Catal. B* **2025**, *366*, 125007. [CrossRef]
56. Wu, D.; Zhuo, Z.; Song, Y.; Rao, P.; Luo, J.; Li, J.; Deng, P.; Yang, J.; Wu, X.; Tian, X. Synergistic Spin-Valence Catalysis Mechanism in Oxygen Reduction Reactions on Fe-N-C Single-Atom Catalysts. *J. Mater. Chem. A* **2023**, *11*, 13502–13509. [CrossRef]
57. Xie, H.; Du, B.; Huang, X.; Zeng, D.; Meng, H.; Lin, H.; Li, W.; Asefa, T.; Meng, Y. High Density Single Fe Atoms on Mesoporous N-Doped Carbons: Noble Metal-Free Electrocatalysts for Oxygen Reduction Reaction in Acidic and Alkaline Media. *Small* **2023**, *19*, 2303214. [CrossRef]
58. He, Y.; Yang, X.; Li, Y.; Liu, L.; Guo, S.; Shu, C.; Liu, F.; Liu, Y.; Tan, Q.; Wu, G. Atomically Dispersed Fe-Co Dual Metal Sites as Bifunctional Oxygen Electrocatalysts for Rechargeable and Flexible Zn–Air Batteries. *ACS Catal.* **2022**, *12*, 1216–1227. [CrossRef]
59. Karimi-Maleh, H.; Karaman, C.; Karaman, O.; Karimi, F.; Vasseghian, Y.; Fu, L.; Baghayeri, M.; Rouhi, J.; Kumar, P.S.; Show, P.-L.; et al. Nanochemistry Approach for the Fabrication of Fe and N Co-Decorated Biomass-Derived Activated Carbon Frameworks: A Promising Oxygen Reduction Reaction Electrocatalyst in Neutral Media. *J. Nanostruct. Chem.* **2022**, *12*, 429–439. [CrossRef]
60. Li, H.; Wen, Y.; Jiang, M.; Yao, Y.; Zhou, H.; Huang, Z.; Li, J.; Jiao, S.; Kuang, Y.; Luo, S. Understanding of Neighboring Fe-N4-C and Co–N4–C Dual Active Centers for Oxygen Reduction Reaction. *Adv. Funct. Mater.* **2021**, *31*, 2011289. [CrossRef]
61. Li, Y.; Ding, Y.; Zhang, B.; Huang, Y.; Qi, H.; Das, P.; Zhang, L.; Wang, X.; Wu, Z.-S.; Bao, X. N,O Symmetric Double Coordination of an Unsaturated Fe Single-Atom Confined within a Graphene Framework for Extraordinarily Boosting Oxygen Reduction in Zn–Air Batteries. *Energy Environ. Sci.* **2023**, *16*, 2629–2636. [CrossRef]
62. Sheng, J.; Zhu, S.; Jia, G.; Liu, X.; Li, Y. Carbon Nanotube Supported Bifunctional Electrocatalysts Containing Iron–Nitrogen–Carbon Active Sites for Zinc–Air Batteries. *Nano Res.* **2021**, *14*, 4541–4547. [CrossRef]
63. Yang, Q.; Liu, R.; Pan, Y.; Cao, Z.; Zuo, J.; Qiu, F.; Yu, J.; Song, H.; Ye, Z.; Zhang, S. Ultrahigh-Loaded Fe Single Atoms and Fe3C Nanoparticle Catalysts as Air Cathodes for High-Performance Zn–Air Batteries. *ACS Appl. Mater. Interfaces* **2023**, *15*, 5720–5731. [CrossRef]
64. Wu, Y.; Liu, J.; Sun, Q.; Chen, J.; Zhu, X.; Abazari, R.; Qian, J. Molecular Catalyst of Fe Phthalocyanine Loaded into In-Based MOF-Derived Defective Carbon Nanoflowers for Oxygen Reduction. *Chem. Eng. J.* **2024**, *483*, 149243. [CrossRef]
65. Li, T.; Lu, Y.; Zhao, S.; Gao, Z.-D.; Song, Y.-Y. Co_3O_4-doped Co/CoFe nanoparticles encapsulated in carbon shells as bifunctional electrocatalysts for rechargeable Zn–Air batteries. *J. Mater. Chem. A* **2018**, *6*, 3730–3737. [CrossRef]
66. Liang, Y.; Wang, H.; Diao, P.; Chang, W.; Hong, G.; Li, Y.; Gong, M.; Xie, L.; Zhou, J.; Wang, J.; et al. Oxygen Reduction Electrocatalyst Based on Strongly Coupled Cobalt Oxide Nanocrystals and Carbon Nanotubes. *J. Am. Chem. Soc.* **2012**, *134*, 15849–15857. [CrossRef]
67. Han, X.; Yu, C.; Yang, J.; Zhao, C.; Huang, H.; Liu, Z.; Ajayan, P.M.; Qiu, J. Mass and Charge Transfer Coenhanced Oxygen Evolution Behaviors in CoFe-Layered Double Hydroxide Assembled on Graphene. *Adv. Mater. Interfaces* **2016**, *3*, 1500782. [CrossRef]
68. Öztürk, A.; Bayrakçeken Yurtcan, A. Preparation and characterization of melamine-led nitrogen-doped carbon blacks at different pyrolysis temperatures. *J. Solid State Chem.* **2021**, *296*, 121972. [CrossRef]
69. He, C.; Xia, C.; Li, F.-M.; Zhang, J.; Guo, W.; Xia, B.Y. Rational Design of Oxygen Species Adsorption on Nonnoble Metal Catalysts for Two-Electron Oxygen Reduction. *Adv. Energy Mater.* **2024**, *14*, 2303233. [CrossRef]
70. Song, W.; Ren, Z.; Chen, S.-Y.; Meng, Y.; Biswas, S.; Nandi, P.; Elsen, H.A.; Gao, P.-X.; Suib, S.L. Ni- and Mn-Promoted Mesoporous Co_3O_4: A Stable Bifunctional Catalyst with Surface-Structure-Dependent Activity for Oxygen Reduction Reaction and Oxygen Evolution Reaction. *ACS Appl. Mater. Interfaces* **2016**, *8*, 20802–20813. [CrossRef] [PubMed]

Disclaimer/Publisher's Note: The statements, opinions and data contained in all publications are solely those of the individual author(s) and contributor(s) and not of MDPI and/or the editor(s). MDPI and/or the editor(s) disclaim responsibility for any injury to people or property resulting from any ideas, methods, instructions or products referred to in the content.